Accounting for Tropospheric Anomalies in High Integrity and High Accuracy Positioning Applications

Samer Khanafseh, Mathieu Joerger and Boris Pervan, *Illinois Institute of Technology*
Axel Von Engeln, *EUMETSAT*

ABSTRACT

This paper describes and quantifies the impact of tropospheric duct anomalies on the integrity risk of a high accuracy differential satellite-based navigation system. First, tropospheric ducts are defined, their causes are identified and their effects on differential satellite ranging signals are analyzed. Second, an error model for tropospheric duct is derived and a threat space is developed using 10 years of troposphere observations. Third, two approaches are introduced to establish protection level equations in the presence of tropospheric duct anomalies: a bounding bias approach and a more conservative, but less constraining sigma-inflation method. Finally, performance evaluations are carried out for an example aircraft shipboard landing application.

INTRODUCTION

The troposphere is the lowest part of the earth's atmosphere, extending from earth surface to about 16 km altitude. It is made of electrically neutral gases that are not uniform in composition, including water vapor and dry gases. Refraction in the troposphere delays the transmission of satellite signals. The tropospheric delay consists of a largely predictable dry component, and of a wet component that varies with latitude, altitude, season, and weather condition but represents a much smaller fraction of the error. Therefore, the majority of the tropospheric delay can be removed by troposphere modeling. Several models exist that describe the tropospheric delay under nominal conditions. These models include, but are not limited to, Hopfield, Modified Hopfield, and Saastamoinen Models [1].

For differential satellite ranging implementations, a nominal model of differential tropospheric delays was defined in the context of the Local Area Augmentation System (LAAS). In this model, the refractivity is expressed in terms of reference refractivity N_r, scale height h_0 and antenna height z as [8]:

$$N = N_r \exp\left(\frac{-z}{h_0}\right) \quad (1)$$

The differential tropospheric delay is then evaluated by integrating N in Equation 1 from the height of the ground station to that of the aircraft, which results in

$$T = 10^{-6} N_r h_0 \left(1 - e^{-\Delta h / h_0}\right) \quad (2)$$

where Δh is the height difference between the aircraft and ship. Equation 2 is used to correct differential measurements under nominal tropospheric condition. In addition, the standard deviation σ_{Trop} of the estimated delay T is derived in reference [8] in terms of the uncertainty in N (with standard deviation σ_N) (Equation 3).

$$\sigma_{Trop} = 10^{-6} \sigma_N h_0 \left(1 - e^{-\Delta h / h_0}\right) \quad (3)$$

Because the correction in Equation 2 is used in the measurement domain, σ_{Trop} can be root-sum-squared (RSS) with the measurement noise standard deviation.

In this work, we investigate the potential of differential carrier phase navigation architectures [2-7] to meet stringent requirements in both accuracy and integrity. We evaluate the impact of residual tropospheric errors, after the nominal tropospheric correction (T in Equation 2) has been removed. Residual errors can be caused by anomalous tropospheric phenomena causing the delay to differ from the model expressed in Equation 2. There are two types of tropospheric anomalies that affect differential systems: horizontal tropospheric anomalies (caused by weather fronts) and vertical tropospheric anomalies (caused by tropospheric ducts) (Figure 1).

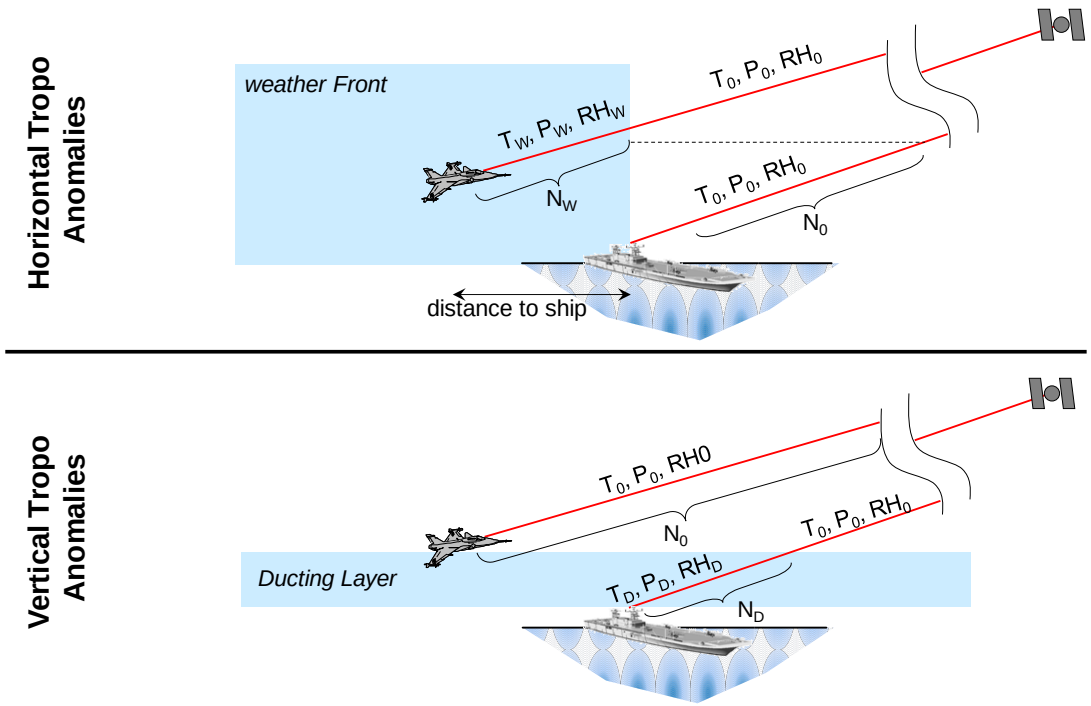

Figure 1: Two Types of Tropospheric Anomalies: Horizontal and Vertical Anomalies.

A weather front is characterized by an abrupt change in refractivity (measured by variations in temperature, pressure, and relative humidity) over short horizontal distances. Published research reports experimental observations of tropospheric delays of up to 40 cm over a 5-km distance [9]. Further published work, with application to ground based augmentation systems (GBAS), assumed a 'weather-wall' model to investigate the impact of high stationary fronts on differential ranging measurements (between a user and a local reference station) [10]. Reference [10] addresses this source of error, showing that non-nominal differential tropospheric errors can be accounted for using a bounding tropospheric decorrelation parameter (i.e., a tropospheric delay gradient over user-to-reference separation distance). The focus of this work is on vertical tropospheric anomalies.

In the next sections of this paper, vertical tropospheric anomalies or ducts are defined. We describe their causes, and explain their influence on the refractivity index using illustrative examples extracted from a set of experimental data. Ducts are shown to be potential integrity threats because they can cause large measurement errors relative to differential carrier phase tracking noise, and because they have a high likelihood of occurrence. Years of tropospheric observations collected at multiple locations are then processed to quantify the impact of ducts on satellite ranging signals. A simplified three-parameter 'wedge model' is derived, which enables to establish a duct threat model in the form of a ranging measurement error probability distribution. These ranging errors are conservatively accounted for using two methods that we develop to evaluate the ducts impact on position estimates and on protection levels. Finally, we analyze the impact of tropospheric anomalies using the two methods for an example shipboard landing application.

TROPOSPHERIC DUCTS

Under nominal tropospheric conditions, pressure drops exponentially with height, and temperature decreases with altitude at an approximate rate of 1K/100m (over the first few kilometers above sea level). As a result, the computed refractivity gradient over altitude (in Equation 1) is approximately -40/km. However, this standard behavior does not apply under anomalous atmospheric conditions when tropospheric ducts can be generated. Ducts tend to form when either temperature is increasing, or water vapor concentration is decreasing with height, or both. Mechanisms causing the apparition of ducts include:

1- Temperature inversion: usually, temperature falls with height by about 1K per 100m. In a temperature-inversion layer, the temperature rises with height. For example, on a clear night the ground cools faster causing the air at the surface to be lower in temperature than at higher altitudes.

2- Evaporation ducts: is associated with the sharp drop in moisture above a water surface. It results from

the evaporation of water vapor, which causes the water vapor pressure at the sea surface to be saturated while the layer above contains less moisture. The resulting humidity gradient is usually sufficient to maintain a surface duct above the sea surface. This usually occurs over large expanses of water such as the great lakes.

3- Air subsidence: this is a mechanism that can lead to elevated ducts and is associated with high pressure weather systems such as anticyclones. Descending cold air forced downwards by the anticyclone heats up as it is being compressed and becomes warmer than the air near the ground, which leads to an elevated temperature inversion. As the anticyclone evolves, the air at the edges subsides which brings the inversion layer closer to the ground. As a result, the inversion layer becomes lower close to the edge of the anticyclone and higher in the middle.

4- Air advection: this phenomenon occurs when air moves from warm land to cooler sea surface typically in early evenings in summer. This warm air mixes with the cooler moist air over the sea causing the height of the evaporation duct to increase. This also leads to high humidity gradients and a temperature inversion. As a result, a surface duct within the first few 100 meters above the sea is formed. These ducts usually occur over the coastal regions.

Due to the sudden change in temperature and relative humidity caused by ducts, the refractivity will not follow the nominal exponential curve in Equation 1. Refractivity data from the European Centre for Medium range Weather Forecast (ECMWF) are shown in Figure 2 [11] (Note: we use the ERA-Interim re-analysis here, [11] was based on ERA-40). The figure shows examples of refractivity profiles in the presence of ducts at two different locations. It is obvious from the figure that the refractivity gradient when ducts exist (blue curves) is much higher than the nominal case (red curves). In Figure 2-a, the refractivity profile gets back to nominal values right after the initial duct gradient while in Figure 2-b, the convergence between the blue and red curves is quite slow.

We now consider the impact of such ducts on radiofrequency signals. For simplicity, and assuming that the reference station is at zero height, the differential tropospheric delay at any height is the integration of each curve with respect to height. The tropospheric error due to the existence of ducts will therefore be the difference between the two integrals (i.e., the area between the nominal refractivity curve (red) and the duct refractivity curve (blue)). Figure 3 shows the profile of the residual tropospheric error (after removing the nominal tropospheric correction from the data) corresponding to Figure 2-a. Figure 3 illustrates that the zenith error caused by the duct reaches up to 1 cm. Tropospheric errors affecting satellite signals can be scaled by an obliquity factor to model the fact that low-elevation ranging signals travel across larger sections of the troposphere than high-elevation observations. Taking the obliquity factor into account, an error magnitude of 1 cm in zenith corresponds to a measurement error of 7.7 cm for a 7 degree elevation satellite. Therefore, the duct error affecting carrier phase measurements is much larger than the magnitude of the measurement noise itself (which is in the order of 1 cm).

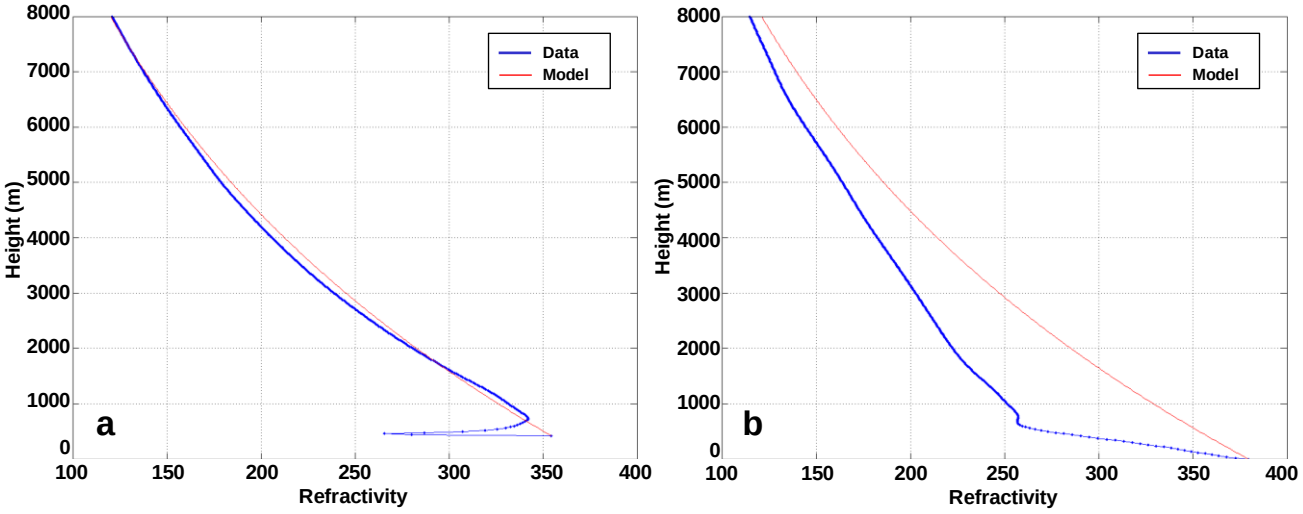

Figure 2: Refractivity Profiles at Two Different Locations (a:25N 97E and b:27N 51E) in the Presence of Ducts. Blue: Refractivity from the ECMWF Model; Red: Nominal Exponential Profile.

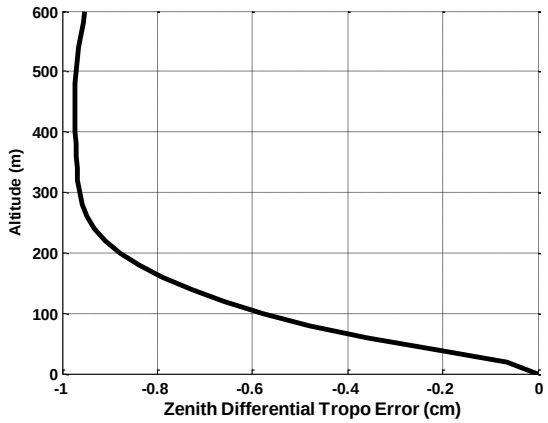

Figure 3: Zenith Differential Tropospheric Error for the First 600 m of the Profile in Figure 2-a.

In addition to the duct error magnitude, another parameter of interest when modeling that type of anomalies is the likelihood of occurrence of ducts. In [11], six years of ECMWF data were analyzed and several duct characteristics were reported. In particular, a global map of duct likelihood of occurrence was established. However, these results included all ducts at all altitudes.

For most aircraft approach applications, and in particular the shipboard landing application , tight integrity and accuracy requirements are only required close to the ship and at low altitudes (for example, around 200 m altitude). Therefore, if a duct exists at an altitude higher than 200 m, it will be eliminated in the differential process and will not pose any integrity threat. Only ducts that are lower than 200 m will cause modeling errors that might jeopardize integrity. Therefore, a new map of duct likelihood of occurrence is generated in Figure 4 using 10 years of ECMWF data (2000-2009). In this map, only ducts occurring below 200 m are considered. The map illustrates that the likelihood of a duct happening below 200 m is much larger than the integrity risk requirement demanded in most aviation applications. Therefore, the duct's high probability of occurrence combined with its large error magnitude (relative to carrier phase measurement noise) causes it to be a substantial threat for GNSS-based aviation applications.

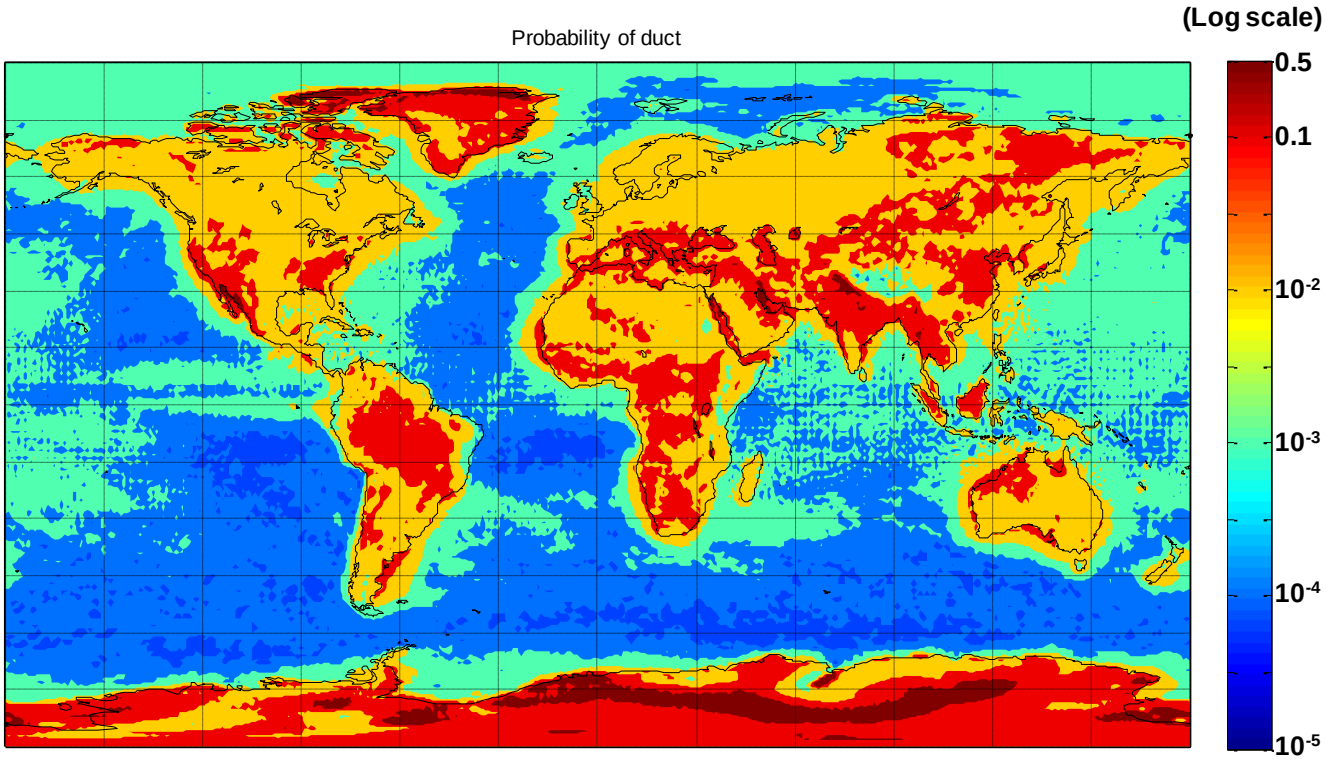

Figure 4: Map of the Ducts' Likelihood of Occurrence

TROPOSPHERIC DUCT THREAT MODEL

The multiple atmospheric parameters influencing a duct and their large range of variation make the definition of a threat model challenging. One approach would be to compute the tropospheric delays caused by each one of the ducts observed in the 10 years of data (analyzed in the previous section), but this would be computationally

extremely demanding. Instead, a simplified duct model that only depends on three parameters is defined. Figure 5 shows the duct 'wedge model', which is defined using the duct altitude (where the duct steep gradient in refractivity starts), duct thickness (the region where the duct gradient is steep, i.e., lower than -100/km), and duct gradient (the average slope of the duct). Using these parameters and the wedge model, the mismodeling residual error due to tropospheric ducts can be analytically determined by computing the area of the triangle (shaded in yellow). It is acknowledged that this model is optimistic because it assumes that once the duct ends, it instantaneously recovers nominal profile values. This assumption may not be realistic according to Figure 2. However, this preliminary analysis will provide useful information towards establishing the severity of the threat that ducts represent. A refined model will be considered in the future.

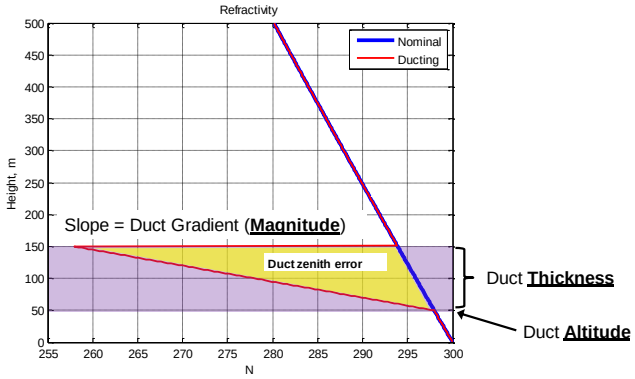

Figure 5: Three-Parameter Wedge Model Used to Account for Ducts

In this paper, we selected six different locations around the US (displayed in Figure 6) and used the 10 years of ECMWF data to record the duct parameters (presented in Figure 7). To create a threat model, the thickness, gradient and altitude parameters illustrated in Figure 7 must be combined. Considering extreme parameter values would be overly-conservative: large duct gradients only occur for small thicknesses; also, thick duct layers are only observed for small gradient magnitudes. Instead, we establish a threat model that is based on residual measurement errors directly derived from the parameter combinations displayed in Figure 7. Using these parameters and assuming that the integration is performed at the highest altitude considered here (200 m), the duct error is computed. The tropospheric zenith errors computed based on the wedge model parameter values in Figure 7 are then used to generate the histogram in Figure 8. This histogram shows that for these six locations and for the wedge model, the maximum error that was observed at 200 m is 6 mm in zenith (approximately 5 cm for a 7 degree elevation satellite signal). The histogram also shows that the duct error distribution is non Gaussian and is non zero mean. Therefore, duct errors cannot simply be accounted for by inflating the measurement error standard deviation. In this work, two different approaches are proposed: a bounding bias approach and a sigma inflation approach.

Figure 6: Locations Where Data Was Collected to Generate a Preliminary Threat Model

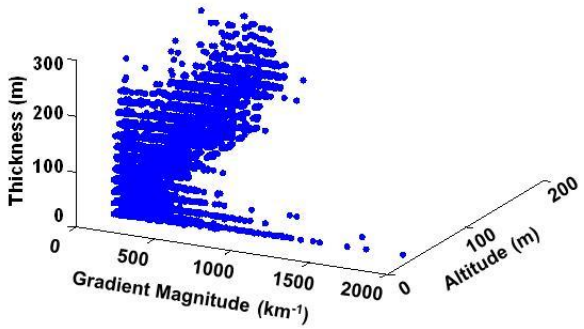

Figure 7: Duct Altitudes, Thicknesses, and Gradient Magnitudes Recorded Over 10 Years at the Six Locations Indicated in Figure 6.

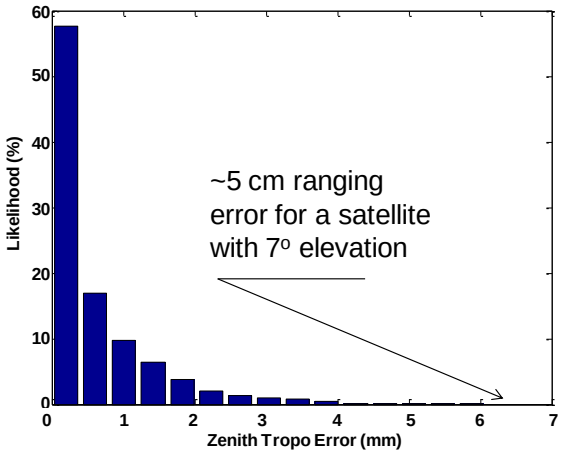

Figure 8: Histogram of the Zenith Tropospheric Error Observed Over 10 Years At the Six Selected Locations.

BOUNDING BIAS APPROACH

In this approach, the worst case duct bias is used as a bound γ for all zenith duct errors d.

$$|d| \le \gamma \tag{4}$$

For example, in Figure 8, the worst case bias of 6 mm is used as a bound on the zenith tropospheric error at 200 m altitude. The delay is then assumed to linearly decrease from that value at 200 m altitude to zero at touchdown. Using this bound is conservative because it converts the histogram in Figure 8 to a single bin at that error value with 100% probability. This measurement error bound will be used to provide a bound on the mean of the differential position estimate error.

Multiplying the zenith error d by the vector $\mathbf{a}$ of obliquity factors for each satellite results in the duct error vector $\delta\mathbf{T}$ (in the measurement domain).

$$\delta\mathbf{T} = \mathbf{a}d \tag{5}$$

Using the definition of the bound in Equation 4, the tropospheric error is bounded as,

$$|\delta\mathbf{T}| \le \mathbf{a}\gamma \tag{6}$$

If a least squares estimator is used to compute the aircraft position, the mean $\delta\hat{\mathbf{x}}$ of the position estimate error can be written in terms of the pseudo inverse matrix $\mathbf{H}^+$ as,

$$\delta\hat{\mathbf{x}} = \mathbf{H}^+\delta\mathbf{T} = \mathbf{H}^+\mathbf{a}d \tag{7}$$

where $\mathbf{H}^+ = \left(\mathbf{H}^T\mathbf{R}^{-1}\mathbf{H}\right)^{-1}\mathbf{H}^T\mathbf{R}^{-1}$, $\mathbf{H}$ is the observation matrix and $\mathbf{R}$ is the measurement noise covariance matrix.

Using the inequality in Equation 6, a bound $\overline{\delta\hat{\mathbf{x}}}$ on the mean of the estimate error can be achieved as

$$\overline{\delta\hat{\mathbf{x}}} = \mathbf{H}^+\mathbf{a}\gamma \tag{8}$$

Such that $\overline{\delta\hat{\mathbf{x}}} \ge \delta\hat{\mathbf{x}}$.

By extracting the element that corresponds to the vertical component ($\overline{\delta\hat{x}_v}$) from $\overline{\delta\hat{\mathbf{x}}}$, the vertical protection level given the duct hypothesis VPL_{Hd} is computed as,

$$VPL_{Hd} = \overline{\delta\hat{x}_v} + k_{Hd}\sigma_v \tag{9}$$

k_{Hd} in Equation 9 is the integrity multiplier. Given a duct hypothesis probability P_{Hd}, it is computed using the inverse of the Gaussian cumulative distribution function Φ and the fault-free integrity risk requirement I_{H0} as:

$$k_{Hd} = \Phi^{-1}\left(\frac{I_{H0}P_{Hd}}{2}\right) \tag{10}$$

The final *VPL* is the maximum of the fault-free and duct-free *VPL* (VPL_{H0nd}) and VPL_{Hd}. These *VPL* equations can be included in the airborne navigation system architecture to account for tropospheric duct anomalies. For practical applications, modifying the airborne algorithm might not be feasible. In this case, an alternative approach of inflating the measurement noise standard deviation is developed.

SIGMA INFLATION APPROACH

In this approach, the standard deviation (sigma) of the measurement noise used in protection level equations is inflated to take the tropospheric anomalies into account. In other words, the inflated sigma must provide a *VPL* that is greater than or equal to the one in Equation 9. We will consider cases where the inflated sigma is either computed as a side-process on the airborne system or where it is broadcasted from the ship. The first step in deriving the inflated sigma is to equate the new *VPL* using the inflated sigma scaled by the fault free integrity risk multiplier k_{H0} with the one from Equation 9.

$$k_{H0}\overline{\sigma_v} = \overline{\delta\hat{x}_v} + k_{Hd}\sigma_v \tag{11}$$

where $\overline{\sigma_v}$ is the standard deviation of the vertical position estimate error that was computed based on the inflated measurement sigma $\overline{\sigma_\phi}$. In order to derive a formula for $\overline{\sigma_\phi}$, we start by writing $\overline{\sigma_v}$ in terms of the corresponding measurement noise standard deviations and pseudoinverse matrix $\mathbf{H}^+$ as,

$$\overline{\sigma_v} = \left\|\mathbf{H}^+_{3,:}\right\|_2 \overline{\sigma_\phi} \tag{12}$$

where $\mathbf{H}^+_{3,:}$ is the third raw of the pseudoinverse matrix and $\|\bullet\|_i$ is the ith norm. A similar equation can be written for σ_v:

$$\sigma_v = \left\|\mathbf{H}^+_{3,:}\right\|_2 \sigma_\phi \tag{13}$$

The term $\overline{\delta\hat{x}_v}$ can be written as

$$\overline{\delta \hat{x}_v} = \left\| \mathbf{H}^{+}_{3,:} \mathbf{a} \right\|_1 \gamma \tag{14}$$

Substituting Equation 12, 13 and 14 in 11 and solving for $\overline{\sigma_\phi}$ results in:

$$\overline{\sigma_\phi} = \frac{\left\| \mathbf{H}^{+}_{3,:} \mathbf{a} \right\|_1}{k_{H0} \left\| \mathbf{H}^{+}_{3,:} \right\|_2} \gamma + \frac{k_{Hd}}{k_{H0}} \sigma_\phi \tag{15}$$

In order to compute $\overline{\sigma_\phi}$ without having to change the airborne architecture, the $\mathbf{H}^{+}$ terms in Equation 15 must be eliminated. These terms depend on the aircraft observation matrix, which might not be accessible by the airborne side-process and which is unknown at the ship. However, eliminating $\mathbf{H}^{+}$ terms is not trivial unless conservative bounds are implemented. Using Holder's inequality, the term $\left\| \mathbf{H}^{+}_{3,:} \mathbf{a} \right\|_1$ can be written as

$$\left\| \mathbf{H}^{+}_{3,:} \mathbf{a} \right\|_1 \le \left\| \mathbf{H}^{+}_{3,:} \right\|_2 \left\| \mathbf{a} \right\|_2 \tag{16}$$

Substituting Equation 16 in Equation 15,

$$\overline{\sigma_\phi} \le \frac{\left\| \mathbf{a} \right\|_2}{k_{H0}} \gamma + \frac{k_{Hd}}{k_{H0}} \sigma_\phi \tag{17}$$

Given that the airborne architecture has at least access to the elevation angles of the current constellation, these can be used to estimate $\left\| \mathbf{a} \right\|_2$ and the right hand side in Equation 17 can be used to provide an inflation on the measurement noise standard deviation. This approach is referred to as sigma inflation 'approach-A'. If the inflation of the sigma is required to be accomplished on the ship, where even the elevation angles of the satellites visible to the aircraft are not known, or if it is desired to make it a constant that does not change for different geometries, another conservative inequality can be used such that,

$$\left\| \mathbf{a} \right\|_2 \le \sqrt{n} \max(\mathbf{a}) \tag{18}$$

As a result, Equation 15 becomes:

$$\overline{\sigma_\phi} \le \frac{\sqrt{n} \max(\mathbf{a})}{k_{H0}} \gamma + \frac{k_{Hd}}{k_{H0}} \sigma_\phi \tag{19}$$

The right hand side of Equation 19 can be used at the ship or even as a hard-coded value for the inflated measurement noise standard deviation given duct tropospheric anomalies (referred to as sigma inflation 'approach-B'). For example, if it is assumed that the maximum number of visible satellites is 12, and that the maximum obliquity factor is 7.7 (for 7^o elevation satellite), Equation 19 becomes:

$$\overline{\sigma_\phi} \le \frac{26.7}{k_{H0}} \gamma + \frac{k_{Hd}}{k_{H0}} \sigma_\phi \tag{19}$$

Next, we will analyze these methods by evaluating the impact of tropospheric duct errors on availability for an example shipboard navigation system.

AVAILABILITY SIMULATION

In this section, we quantify the impact of the tropospheric duct on a high integrity and high accuracy navigation system. This navigation architecture under consideration is designed to support a specific application: autonomous shipboard landing. Because of the mobility of the reference station in a shipboard-relative landing application, higher levels of accuracy are required than for similar precision approach applications at land-based airfields. In addition, to ensure safety and operational usefulness, the navigation architecture must provide high levels of integrity and availability. Because of the highly stringent requirements, the navigation system is based on Carrier Phase Differential GPS (CPDGPS) positioning. However in order to benefit from the high precision of CPDGPS the cycle ambiguities must be estimated accurately. A number of methods have been used in prior work to aid in the high-integrity cycle resolution. Satellite motion can provide the observability of the cycle ambiguities [1]. Unfortunately the rate of satellite motion is relatively slow in comparison with the time scales of the mission in considerations.

Heo, et al. have proposed a GPS navigation algorithm for autonomous shipboard landing applications where geometry-free/divergence-free code-carrier filtering is performed continuously for visible satellites on both the aircraft and the ship until the aircraft is close to the ship [2]. Geometry-free filtering [6], by definition, does not depend on the geometry of the satellites or the user location and eliminates major error sources such as atmospheric errors, clock and ephemeris errors and leaves relatively small errors such as receiver noise and multipath. A geometry free measurement of the widelane cycle ambiguity is formed by subtracting the narrowlane pseudorange from the widelane carrier [1, 6]. A drawback of the geometry free measurement is the presence of higher noise caused by the combination of L1 and L2 carrier phase measurements. This drawback can be overcome by filtering the geometry free measurement over time prior to the final approach. In order to model colored multipath noise in the geometry free measurements, a first order Gauss-Markov measurement error model is used. In this work, a time constant of one minute for the ship and 30 seconds for aircraft is assumed.

The outputs of the filtering process are the floating widelane cycle ambiguity estimates. When the aircraft is close to the ship, floating L1/L2 cycle ambiguity estimates can be extracted with the aid of satellite geometric redundancy [2, 5, 7]. In this work the ambiguities are left as float numbers (they are not fixed) because a method to account for faults using a cycle resolution process has not been developed yet.

Therefore, the performance can be predicted for a single aircraft approach by covariance analysis. To account for the GPS satellite geometry change, availability analysis is performed by simulating 1440 approaches (one approach per minute during the day). In this work, a straight in approach (Case-III landing approach) is assumed. A given approach is said to be available if the integrity requirements are satisfied at each point along the approach. Availability is calculated as the percentage of approaches for which *VPL* (in this case VPL_{Hd}) during the entire approach is less than *VAL*. For the autonomous shipboard landing application, *VAL* varies as functions of distance to touchdown as shown in Figure 9. The *VAL* is the most stringent at the touch-down point, where aircraft positioning errors are the most hazardous.

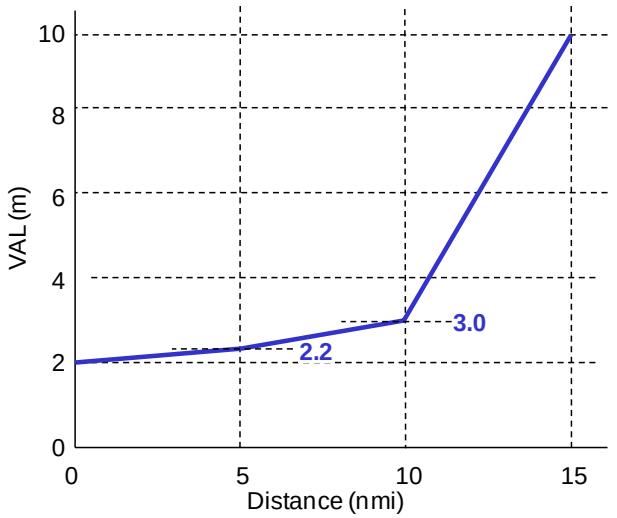

Figure 9: VAL Requirement as a Function of Distance to Touch Down

In this work, the requirements and simulation parameters are based on those given in [2] and [4]. The standard deviation of the carrier phase measurement noise is assumed to be 7 mm and the standard deviation of the pseudorange measurement noise is assumed to be 35 cm. Also, geometry-free prefiltering is assumed to start at the beginning of the approach and is used to generate floating estimates of the widelane cycle ambiguities. The rest of the simulation parameters are summarized in Table I. The threat model in the previous section (based on six selected locations across the US) shows a maximum tropospheric delay of 6 mm. Because the analysis was only based on six locations, in this simulation the availability was computed for different zenith duct errors ranging from 0 mm to 3 cm (which encapsulates the observed 6 mm). Maximum duct errors are used at 200 m altitude and decrease linearly to zero at touchdown.

Table 1 Simulation Parameters

Parameters	Nominal Value or Setting
H0 integrity risk allocation	$6x10^{-7} \rightarrow k_{H0}=5$
Duct prior probability	100 % $\rightarrow k_{Hd}=5$
Sigma code, carrier	35 cm, 0.7 cm
Constellation (almanac)	24 SV (DO-229) [12]
Location	37^o North, 74^o West
Elevation angle mask	7^o

Using the simulation parameters given in Table 1, Figure 10 shows the impact of the tropospheric duct error on the example shipboard navigation system using three different approaches: the bounding bias approach (in blue), sigma inflation approach-A (in green), and sigma inflation approach-B (in red). The figure illustrates that the sigma inflation approach-B is overly conservative. It causes availability to rapidly drop to 6% for a zenith duct error of 4 mm. Although the sigma inflation approach-A performs better, zenith error larger than 5 mm causes availability using this conservative error bounding approach to drop below 95%. This error level is still less than what was observed from the threat model in Figure 8. On the other hand, the bounding bias approach provides the best availability over a wide range of zenith errors (up to 3 cm) and only suffers a 1% availability loss while accounting for tropospheric ducts. This outstanding performance comes at the expense of modifying the airborne architecture to include the new VPL equation (Equation 9).

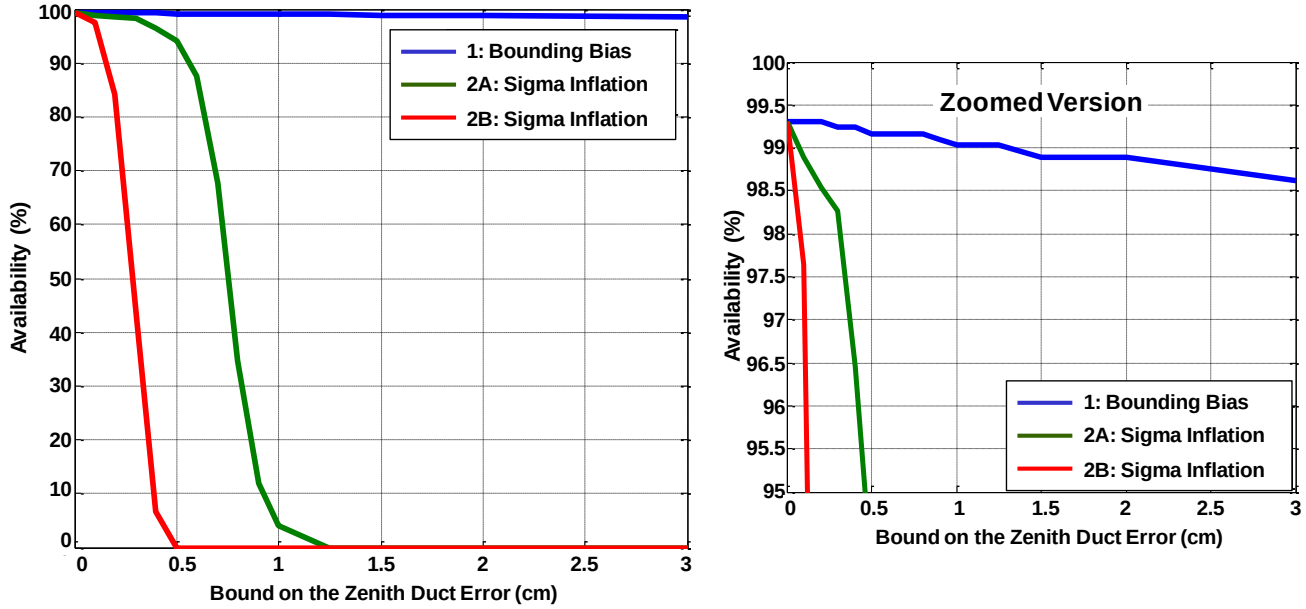

Figure 10: Availability for Different Values of Zenith Duct Error and Using Different VPL Computation Approaches (the Plot on the Right Hand Side is a Zoomed Version of the One on the Left).

CONCLUSIONS

In this paper, we described tropospheric ducts and illustrated the fact that these anomalies can cause errors of up to 7 cm with a likelihood of occurrence that is much larger than the integrity risk of aviation applications (reaching up to 50% at some locations). A preliminary threat model that describes the duct zenith error was established for six locations across the US. A bound on the measurement error was derived based on the worst case zenith duct error. Two methods were developed to account for the impact of these bounded errors on the navigation system integrity risk. The two methods included a bounding bias approach, and a sigma inflation approach (two variants were presented). Availability analysis for a shipboard landing application showed that the sigma inflation approach was overly conservative and might have severe impact on availability. Therefore, the bounding bias approach provides a tighter bound on the estimated position error. But the improvement in availability performance of the bounding bias approach comes at the price of having to modify the airborne algorithm to incorporate the new VPL equation. In future work, the authors will extend the threat model to include all locations globally and will develop a method to account for duct errors in algorithms that involve cycle resolution.

REFERENCES

[1] P. Misra and P. Enge, Global Positioning System signals, Measurements, and Performance. Lincoln, MA: Ganga-Jamuna Press, 2001.

[2] M. Heo, B. Pervan, S. Pullen, J. Gautier, P. Enge, and D. Gebre-Eziabher, "Robust Airborne Navigation Algorithm for SRGPS," *Proceedings of IEEE/ION Position, Location, and Navigation Symposium (PLANS '2004)*, Monterey, CA, Apr. 2004.

[3] S. Khanafseh and B. Pervan, "Autonomous Airborne Refueling of Unmanned Air Vehicles Using the Global Positioning System," *Journal of Aircraft*, Vol. 44, No. 5, Oct. 2007, pp. 1670-1682.

[4] S. Langel, S. Khanafseh, F. C. Chan, B. Pervan, "Cycle Ambiguity Reacquisition in UAV Applications using a Novel GPS/INS Integration Algorithm," *Proceedings of the 2009 International Technical Meeting of the Institute of Navigation ION-ITM 2009*, Anaheim, CA, Jan. 2009.

[5] S. Dogra, J. Wright, and J. Hansen, "Sea-Based JPALS Relative Navigation Algorithm Development," *Proceedings of the 18th International Technical Meeting of the Satellite Division of the Institute of Navigation ION GNSS 2005*, Long Beach, CA, Sept. 2005.

[6] G. A. McGraw, "Generalized Divergence-Free Carrier Smoothing with Applications to Dual Frequency Differential GPS," *NAVIGATION: Journal of Institute of Navigation*, Vol. 56, No. 2, Summer 2009.

[7] Wu, Shuwu, Peck, Stephen R., Fries, Robert M., "Geometry Extra-Redundant Almost Fixed Solutions: A High Integrity Approach for Carrier Phase Ambiguity Resolution for High Accuracy Relative Navigation," *Proceedings of IEEE/ION PLANS 2008*, Monterey, CA, May 2008, pp. 568-582.

[8] McGraw, Gary A., Murphy, Tim, Brenner, Mats, Pullen, Sam, Van Dierendonck, A. J., "Development of the LAAS Accuracy Models," *Proceedings of the 13th International Technical Meeting of the Satellite Division of The Institute of Navigation (ION GPS 2000)*, Salt Lake City, UT, September 2000, pp. 1212-1223.

[9] Huang, Jidong, van Graas, Frank, Cohenour, Curtis, "Characterization of Tropospheric Spatial Decorrelation Errors Over a 5-km Baseline", *NAVIGATION*, Vol. 55, No. 1, Spring 2008, pp. 39-53.

[10] Van *Graas*, F., Zhu, Z., "Tropospheric Delay Threats for the Ground Based Augmentation System," *Proceedings of the 2011 International Technical Meeting of The Institute of Navigation*, San Diego, CA, January 2011, pp. 959-964.

[11] Axel von Engeln, Joao Teixeira, "A Ducting Climatology derived from ECMWF Global Analysis Fields," *J. Geophys. Res.*, 109 (D18), D18104, doi:10.1029/2003JD004380, 2004.

[12] "Minimum Operational Performance Standards for Global Positioning System/Wide Area Augmentation System Airborne Equipment," RTCA Document Number DO-229C, Nov. 2001, Appendix B.5.